

3D Multi-Resolution Optical Flow Analysis of Cardiovascular Pulse Propagation in Human Brain

Zalán Rajna¹, Lauri Raitamaa², Timo Tuovinen², Janne Heikkilä²,
Vesa Kiviniemi², and Tapio Seppänen²

Abstract—The brain is cleaned from waste by glymphatic clearance serving a similar purpose as the lymphatic system in the rest of the body. Impairment of the glymphatic brain clearance precedes protein accumulation and reduced cognitive function in Alzheimer's disease (AD). Cardiovascular pulsations are a primary driving force of the glymphatic brain clearance. We developed a method to quantify cardiovascular pulse propagation in the human brain with magnetic resonance encephalography (MREG). We extended a standard optical flow estimation method to three spatial dimensions, with a multi-resolution processing scheme. We added application-specific criteria for discarding inaccurate results. With the proposed method, it is now possible to estimate the propagation of cardiovascular pulse wavefronts from the whole brain MREG data sampled at 10 Hz. The results show that on average the cardiovascular pulse propagates from major arteries via cerebral spinal fluid spaces into all tissue compartments in the brain. We present an example, that cardiovascular pulsations are significantly altered in AD: coefficient of variation and sample entropy of the pulse propagation speed in the lateral ventricles change in AD. These changes are in line with the theory of glymphatic clearance impairment in AD. The proposed non-invasive method can assess a performance indicator related to the glymphatic clearance in the human brain.

Index Terms—Brain, FMRI, heart, MREG, optical flow.

I. INTRODUCTION

RECENTLY emerged glymphatic brain clearance mechanisms have been shown to use physiological pulsations to clear the brain tissue from metabolic waste materials such as beta-amyloid protein aggregates [1]–[3]. Glymphatic clearance pushes waste to dural lymphatic vessels and finally to cervical lymph nodes. Abnormal glymphatic clearance has been shown in [1] and [2] to cause beta-amyloid aggregation preceding the Alzheimer's disease.

Manuscript received November 30, 2018; accepted March 5, 2019. Date of publication March 15, 2019; date of current version August 30, 2019. This work was supported in part by the Jane and Aatos Erkko Foundation Grant, in part by the Academy of Finland under Terva-Grant 314497, and in part by the Medical Research Center Oulu Grants. (Corresponding author: Zalán Rajna.)

Z. Rajna, J. Heikkilä, and T. Seppänen are with the Center for Machine Vision and Signal Analysis, University of Oulu, 90014 Oulu, Finland (e-mail: zalan.rajna@oulu.fi).

L. Raitamaa, T. Tuovinen, and V. Kiviniemi are with the Oulu Functional Neuroimaging Group, MRC/MIPT, Oulu University Hospital, 90029 Oulu, Finland.

This article has supplementary downloadable material available at <http://ieeexplore.ieee.org>, provided by the author.

Color versions of one or more of the figures in this article are available online at <http://ieeexplore.ieee.org>.

Digital Object Identifier 10.1109/TMI.2019.2904762

In mice, the cardiovascular pulsations have been shown to push water and contrast media from paravascular space into the brain parenchyma via AQP4 aquaporin water channels at the astrocytic endfeet [1], [2]. Cardiovascular pulses drive the glymphatic water from peri-arterial space into the brain [4], [5]. In humans, ultrafast 3D functional brain scanning can detect the cardiovascular pulsations, and results also suggest, that other physiological pulsations, such as the respiratory venous return oscillations and vasomotor waves, may be involved in the glymphatic brain clearance [6].

A failure of the glymphatic clearance has been shown to precede protein accumulations that lead to neuronal tissue inflammation, reduced cognitive functions, and finally, into dementia [1]. To support this, two recent studies have shown that therapeutically increasing the brain amyloid clearance by momentary opening of the blood brain barrier with focused ultrasound (FUS), can remove most of the protein accumulations and restore the memory performance of treated dementia model mice [7], [8]. Due to the arising treatment options, a non-invasive and safe way, like magnetic resonance encephalography (MREG), could be used to locate impaired glymphatic function to target the FUS-treatment.

While more details of the glymphatic system and brain clearance are being discovered in rodents [9], [10], up to now there has been little advance in the evaluation of glymphatic clearance in the human brain. For example in [11] and [12] magnetic resonance (MR) contrast media was administered intra-theccally via lumbar puncture. The MR contrast media flows through paravascular spaces into the brain, and indicates changes within 6-24 hours in contrast media clearance in normal pressure hydrocephalus.

In [13] and [14], physiological pulsations were evaluated in neurodegenerative diseases as regulators of cerebrospinal fluid (CSF) flow, which is part of the glymphatic pathway. There is also prior evidence suggesting that the physiological noise in functional MR imaging (fMRI) signals are altered in dementia [15], [16]. Recently, drug resistant epilepsy linked to glymphatic AQP4 water channel abnormality, was shown in [17] to have abnormal respiratory brain pulsations in addition to cardiovascular pulsation changes.

In general, an efficient diagnostic tool for neurodegenerative diseases is based on detecting the pathophysiological mechanisms of the disease as early as possible. To non-invasively detect altered glymphatic function, it is desired to quantify changes in the driving physiological pulsations. Previously,

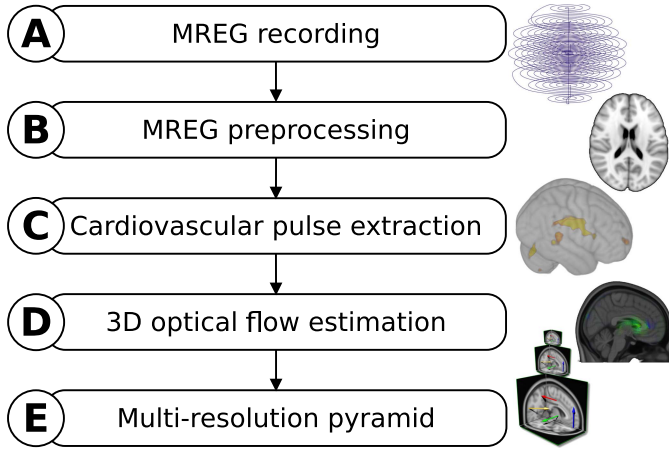


Fig. 1. Overview of the data processing pipeline. Corresponding subsections describing the steps are marked with the same letters within section II.

the driving forces of the glymphatic brain clearance were analyzed in [6] by showing the spreading cardiovascular pulses in healthy human brains with MREG scanning.

In this research, we developed a novel multi-resolution optical flow-algorithm on cardiovascular pulse wavefronts of MREG data with three native spatial dimensions, in order to quantify the propagation of cardiovascular pulsations in the human brain. With the multi-resolution approach, i.e. the hierarchical processing of data as a pyramid of three-dimensional images, the range of accurate flow estimation was extended. Our method is a step towards developing a fast and non-invasive assessment of the glymphatic function.

To prove the feasibility of this new method, we show that the measured flow properties align with the known anatomical structures of the cerebral circulation and CSF pathways. Furthermore, we also show an example area with a significant difference of the measured flow properties between healthy controls and subjects with Alzheimer's, disease (AD). Therefore, the measured properties might be a performance indicator of cardiovascular glymphatic clearance.

II. METHODS

In this study, we developed a three-dimensional generalization of the Lucas-Kanade (LK) optical flow estimation [18] for fast sampled FMRI, with adjustments to the application considering displacement distance and spatial constraints of the brain. An overview of processing steps is presented in Fig. 1.

A. Measurement Data

The MR system is a Siemens 3T SKYRA with a 32-channel head coil. MREG sequence obtained from Freiburg University via collaboration with Jürgen Hennig group [19], [20] was utilized. MREG is a three-dimensional (3D) spiral, single-shot sequence that undersamples 3D k-space trajectory for faster imaging [21]. It samples the brain at 10 Hz frequency ($TR = 100$ ms, $TE = 1.4$ ms, and flip angle = 5°) and offers thus about 20–25 times faster scanning than conventional FMRI. Three-dimensional MPRAGE ($TR = 1900$ ms, $TE = 2.49$ ms, flip angle = 9° , $FOV = 240$, and slice thickness = 0.9) images were used to register the MREG data into 3 mm MNI space. The

high sampling rate of the MREG sequence is crucial to evaluate phenomena in the frequency range of cardiovascular pulsations. While there are a few alternatives for fast sampled FMRI sequences, like [22]–[24], MREG has been proven to be suitable to measure physiological pulsations in [6].

Data was collected from five minutes long resting state MREG measurements from ten healthy control subjects (5 women, 58.3 ± 9.9 years old) and ten age matching subjects with AD (7 women, 60.3 ± 5.0 years old). Dementia was evaluated before each recording with mini-mental state examination (MMSE) as introduced in [25]. Healthy control subjects scored 28.4 ± 1.4 , and AD subjects 22.4 ± 6.6 out of 30 points. The study protocol was approved by the ethics committee of the Northern Ostrobothnia Hospital District. Written informed consent was obtained from each subject individually prior to scanning, in accordance with the Helsinki declaration. During the 5-min MREG resting-state study, subjects were instructed to lie quietly in the scanner with their eyes open fixating at a cross on the screen and thinking nothing particular.

B. Preprocessing Pipeline

MREG data were preprocessed with FSL pipeline in the same way as described by [26]. One hundred and eighty timepoints were removed from the beginning for minimizing T1-relaxation effects. Head motion was corrected with FSL 5.0.11 MCFLIRT software [27].

Brain extraction was carried out after MCFLIRT with optimization of the deforming smooth surface model, as implemented in FSL 5.0.11 BET software [28] using threshold parameters $f = 0.3$ and $g = 0$; and for 3D MPRAGE volumes, using parameters $f = 0.25$ and $g = 0.22$ with neck and bias field correction option. Spatial smoothing was also done with FSL software [28] using 5-mm FWHM Gaussian kernel. Three-dimensional MPRAGE images were used to register the MREG data into MNI space in 3-mm resolution using MCFLIRT in a MELODIC 3.15 pipeline [29].

C. Extraction of Cardiovascular Pulse Wavefronts

To keep the processing steps uniform for all subjects, activity of the brain linked to cardiovascular pulses was extracted with AFNI (Aug 9 2017) [30] 3dTproject bandpass filter (cutoff frequencies: 0.7 Hz, 1.5 Hz). Given the narrow band, the remaining time signal at each voxel is close to sinusoidal.

Wavefronts of the filtered data were extracted in the following way. For every voxel individually, the local maxima were selected, one within each period of the pseudo-sinusoidal signal. All other time points within a period were neglected (replaced with zero), and the maximal value was replaced with the range (maximum – minimum) of the signal within the considered period.

With x being the input signal and y the output signal, and x_t the sample at time point t of x , and y_t similarly of y , the method above can be formulated for a given time point t with

$$y_t = \begin{cases} x_t - x_{t+n} & t \in M \\ 0 & \text{otherwise,} \end{cases} \quad (1a)$$

where n in (1a) at the same time point t is defined as

$$n = \min_n \{n \in \mathbb{N}, (t + n) \in M\} \quad (2)$$

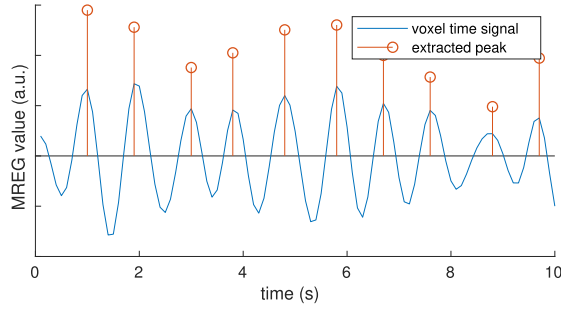


Fig. 2. Wavefront extraction on a time signal of a voxel. Only time points at local maxima have nonzero values, and their value is the distance to the following local minimum.

and M is the array of time points of local maxima, and m is the array of time points of local minima.

Local extrema were selected with the following criteria: there is at least 0.3 seconds distance between the same types of local extrema, furthermore a positive value is required for local maxima, and a negative value is required for local minima. This algorithm is illustrated with an example in Fig. 2.

In practice, this wavefront extraction selects the islands in the brain with highest activity in any given moment, considering the cardiovascular frequencies. In the following steps we estimate their propagation between frames as optical flow.

D. Estimation of Propagation as Optical Flow

The outcome of the algorithm described in this paper, is a three-dimensional vector field between each consecutive three-dimensional data frames. Therefore, at every processing step, i.e. time point, input data are the previous three-dimensional image and the current three-dimensional image.

To estimate the wavefront propagation between time frames, optical flow was measured for each voxel individually, utilizing their $r_{\max} = 2$ neighborhood (L_1 distance). Optical flow was estimated with generalized LK method in a multi-resolution approach, since LK method is optimal if the displacement is of subpixel length. The multi-resolution approach is explained in section II-E.

In this section, we describe briefly the optical flow estimation without the multi-resolution part. Optical flow estimation was performed with LK method, which was extended to three spatial dimensions. For each voxel, we select its $5 \times 5 \times 5$ voxel neighborhood in the current and previous three-dimensional images. Optical flow is estimated between these two $5 \times 5 \times 5$ cubes, and the flow vector is assigned to the middle voxel p .

Equation (3) shows the components of the flow equation $Av = b$,

$$A = \begin{bmatrix} I_x(q_1) & I_y(q_1) & I_z(q_1) \\ I_x(q_2) & I_y(q_2) & I_z(q_2) \\ \vdots & \vdots & \vdots \\ I_x(q_n) & I_y(q_n) & I_z(q_n) \end{bmatrix} \quad v = \begin{bmatrix} V_x \\ V_y \\ V_z \end{bmatrix} \quad b = \begin{bmatrix} -I_t(q_1) \\ -I_t(q_2) \\ \vdots \\ -I_t(q_n) \end{bmatrix} \quad (3)$$

where q_1, q_2, \dots, q_n are voxels in the $5 \times 5 \times 5$ cube, and $I_x(q_i)$, $I_y(q_i)$, $I_z(q_i)$, and $I_t(q_i)$ are the partial derivatives of image I with respect to position x , y , z , and time t , evaluated at point q_i at current time, and v is the flow vector. In our application, the number of voxels involved in estimating flow vector for a single point p is $n = 5^3 = 125$.

Spatial partial image derivatives were calculated with the Sobel operator [31]. This system has more equations than unknowns, thus it is solved by the least squares principle with

$$v = (A^T A)^{-1} A^T b, \quad (4)$$

where matrix $A^T A$ is the structure tensor of point p , for which we calculate optical flow (middle of the cube). If point p is suffering from the aperture problem, the eigenvalues of the structure tensor are small, and the flow vector needs to be discarded. To only include reliable optical flow estimates, the eigenvalues of the second moment matrix (structure tensor) were considered. In case all three eigenvalues were under 1.0, the estimated displacement value was rejected and replaced with zero.

When (4) is solved for all voxels, we obtain a vector field of optical flow, which represents the cardiovascular pulse propagation (wavefront displacement) between the previous and current three-dimensional images.

E. The 3D Multi-Resolution Approach

To overcome the displacement size limitation of LK flow estimation ($r < 1$ voxel) and extend its spatial range r , input data was processed in a multi-resolution manner. In the literature, this method is also referred to as hierarchical processing. Hierarchical processing for LK method is introduced in [32], and it is a well-known approach in computer vision. We developed a 3D extension of multi-resolution LK optical flow estimation.

In short, we first applied the optical flow estimation on a subsampled, lower resolution version of the data, and initialized our higher resolution calculation with the displacement estimation of the previous step. An overview of the recursive algorithm with the multi-resolution approach of flow estimation is presented in Fig. 3. A pseudo-code is shown in Fig. 4. The following few paragraphs present a more detailed explanation of the algorithm.

First, the input data is subsampled multiple times with a factor of two in each spatial dimension, and the flow is estimated in a recursive manner (Fig. 4, line 2). At each resolution step, the flow estimation method is feasible and accurate in subpixel range (e.g. $r < 1$ at scale = 0). At the original resolution (scale = 0), the displacement estimation is accurate only up to one voxel per frame. However, we can initialize the estimation with a coarse displacement estimation (Fig. 4, line 9) and refine it (Fig. 4, line 10), thus taking advantage of the accuracy of the original resolution, without the one voxel per frame being a limitation any more.

To obtain the coarse displacement estimation, we first load the subsampled data (Fig. 4, lines 6-7) at scale = 1. The displacement is accurate up to one voxel per frame between the subsampled images, which is effectively up to two voxels

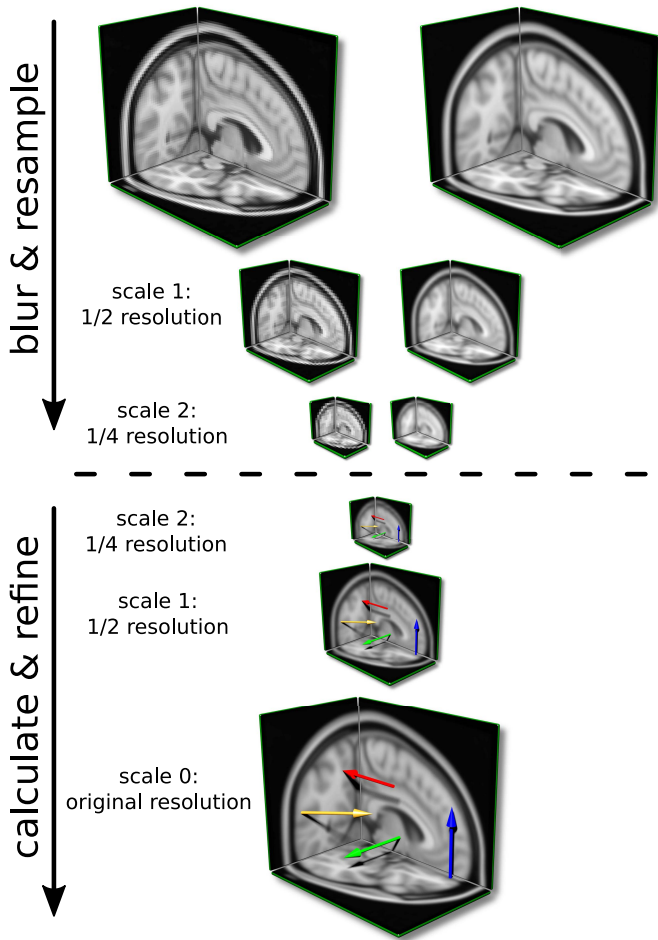


Fig. 3. Multi-resolution pyramid example with three scales. Steps are executed from left to right and top to bottom: blurring (scale 0), resampling (scale 1), blurring (scale 1), resampling (scale 2), blurring (scale 2), coarse flow estimation (scale 2), refined coarse flow estimation (scale 1), refined flow estimation (scale 0).

distance in the original resolution, so now the calculation is feasible if $r < 2$. If we would like to initialize our coarse estimation as well, we obtain the estimation from a further subsampled version of the input data (now scale = 2), and the displacement range of our flow estimation is extended to $r < 4$. With further resampling and coarse initialization steps (scales), this can be calculated as $r < 2^{\text{scale}}$. A desired displacement range r will be the terminating condition of the recursive algorithm.

For each voxel, we select its $5 \times 5 \times 5$ voxel neighborhood in the current three-dimensional image. To calculate the optical flow as described in section II-D, we select the shifted $5 \times 5 \times 5$ voxel neighborhood from the previous three-dimensional image, according to the coarse displacement estimated from a higher scale (lower resolution), or alternatively, zero at lowest resolution (Fig. 4, line 4). In case of non-integer coarse displacement, spline interpolation is applied to extract values corresponding to the desired displacement from the previous image.

In this study, the results were obtained at a multi-resolution scale = 4, i.e. each three-dimensional frame was subsampled four times, thus one voxel distance at the lowest resolution

corresponds to $2^4 = 16$ voxel distance at highest (original) resolution (Fig. 4, line 1). This made the method suitable to estimate bigger displacements.

To ensure accuracy, the resulting vector field was cleaned from displacement values bigger than $2^{\text{scale}+1}$, $2^5 = 32$ at scale = 4. Values over this cannot be accurately estimated with LK method, therefore they were discarded (replaced with zero).

F. Verification With Simulation

In this section we show, that in general, the previously described method is accurate enough if the displacement to be estimated is smaller than $2^{\text{scale}+1}$. The ground truth, i.e. real cardiovascular pulse propagation has been unknown for real MREG data, so validation of the method with simulation was a natural choice.

Simulation was performed with the following protocol. Two frames of three dimensional zero images were generated initially with the size of 64 voxels in each spatial dimension. A centered three dimensional Gaussian function was sampled on the first image grid. A random displacement vector was generated, and a three dimensional Gaussian function displaced with the random vector was sampled on the second image grid. This data was saved to the standard NIFTI file format, and our multi-resolution optical flow estimation algorithm, described in sections II-D and II-E, was used with different number of scales to estimate the optical flow in the central voxel location. Root mean square error (RMSE) was calculated between the random displacement vector, and the calculated optical flow. This was repeated thousands of times focusing on different displacement ranges.

An example for a single simulation is depicted in Fig. 5. The random displacement vector generated in the example was $(-2.206, -1.284, 2.314)$, and the estimates with different maximal scales (from no multi-resolution to three additional resolution scales) are shown in the figure.

It is clear, that in this example, the displacement length of 3.45 suffers from the aperture problem in the local neighborhood. With using only the three-dimensional LK method (scale_{max} = 0), the estimated optical flow value was zeroed, because all eigenvalues in the structure tensor were under 1.0. However, with the multi-resolution approach, the added scales extend the analyzed neighborhood, therefore the estimate becomes reliable, and with more fine-tuning steps (scales) even more accurate.

In Table I we show the smallest displacement lengths found during the simulations, for which the optical flow estimation exceeded the RMSE thresholds 0.01, 0.1, and 1. Considering the MREG spatial sampling grid having 3 mm voxel distances, an estimate with RMSE lower than 0.1 is pretty accurate, the error is typically well within submillimeter distance. It is clear, that with additional multi-resolution scales, the estimates are improving, and larger displacements are estimated accurately. With this simulation we have shown, that the presented method is capable of estimating optical flow accurately enough for our application if the displacement is smaller than $2^{\text{scale}+1}$.

To sum up section II, with our method we obtain a three-dimensional vector field between each time frame of the input

```

1:  $r = 16$ 
2: function PROCESS_MULTIRESCALE(scale, volume1, volume2)
3:   if scale >  $\log_2(r)$  then
4:     return Vector_Field_3D(0)
5:   end if
6:   small_volume1 = BLUR_AND_SUBSAMPLE(volume1)
7:   small_volume2 = BLUR_AND_SUBSAMPLE(volume2)
8:   small_coarse_flow = PROCESS_MULTIRESCALE(scale + 1, small_volume1, small_volume2)
9:   coarse_flow = UPSAMPLE(small_coarse_flow)
10:  refined_flow = CALCULATE_FLOW(coarse_flow, volume1, volume2)
11:  return refined_flow
12: end function
13: flow_vector_field = PROCESS_MULTIRESCALE(0, previous_volume, current_volume)

```

Fig. 4. Pseudo-code of the recursive implementation of optical flow estimation with the multi-resolution approach.

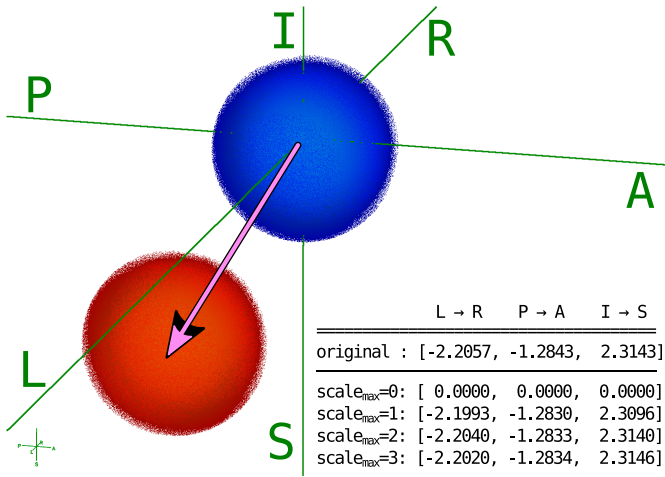


Fig. 5. Simulation example. Axis labels L, R, P, A, I, and S stand for left, right, posterior, anterior, inferior, and superior, respectively. Data in the first and second frames, with manually selected threshold applied, are shown with blue and red colors, respectively. Optical flow was estimated for the example displacement with different number of multi-resolution scales processed.

TABLE I
DISPLACEMENT ESTIMATION SIZE LIMITS WITH DIFFERENT
MULTI-RESOLUTION SCALES AND RMSE THRESHOLDS

RMSE threshold	0.01	0.1	1
scale _{max} = 0	0.816	1.884	4.153
scale _{max} = 1	3.278	5.405	8.782
scale _{max} = 2	9.835	11.551	11.800
scale _{max} = 3	10.699	17.108	17.437

MREG data. This vector field is an estimation of cardiovascular pulse propagation in the human brain at each time point. To demonstrate the value of the extracted pulse propagation data, we both show the long-term directional accuracy of the method, and a significant difference in dynamic flow properties of the lateral ventricles in Alzheimer's disease.

III. RESULTS

The method presented in this paper enables the detection of three-dimensional cardiovascular pulse propagation in the brain. We have identified the amplitude peaks of individual wavefronts and then used optical flow estimation with

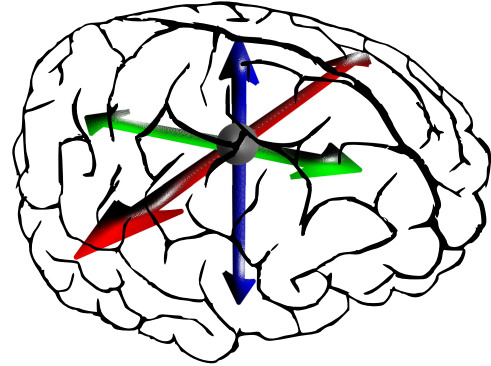


Fig. 6. Color coding of directions. 3D directions are represented on RGB color scale according to MNI coordinate order: red (left-right), green (anterior-posterior), and blue (superior-inferior).

Lucas-Kanade method to quantify the pulse propagation vectors in MNI space.

A. Directional Accuracy—Matching Brain Anatomy

First, we demonstrate the accuracy of the long-term average of pulse propagation directions with matching them to the anatomy of cerebral circulation: brain arteries and veins. Color coding of directions matches the diffusion MRI conventions, the three orthogonal directions are presented with their matched colors in Fig. 6. The color of an arbitrary direction is the linear combination of the three orthogonal colors weighted according to the direction vector's coordinates.

In Fig. 7 and Fig. 8, the direction and strength of cardiovascular pulse propagation is presented as an average of ten healthy control subjects. Mean cardiovascular pulse vector map shows prominent vectors along CSF spaces and periarterial and peri-venous spaces of major vessels as pulse conducts around the brain. A better understanding of this can be obtained from the supplementary video presenting sagittal brain sections consecutively. The arteries present the clearest vector mappings where the pulse propagation maps follow the vessels path with great anatomical detail. Pericallosal A3-A4 arteries and branches of M3-4 segments of medial cerebral artery are most pronounced, as well as areas around basilar artery. Notably, the posterior cerebellar arteries do not present as clear pulses as the medial and anterior areas.

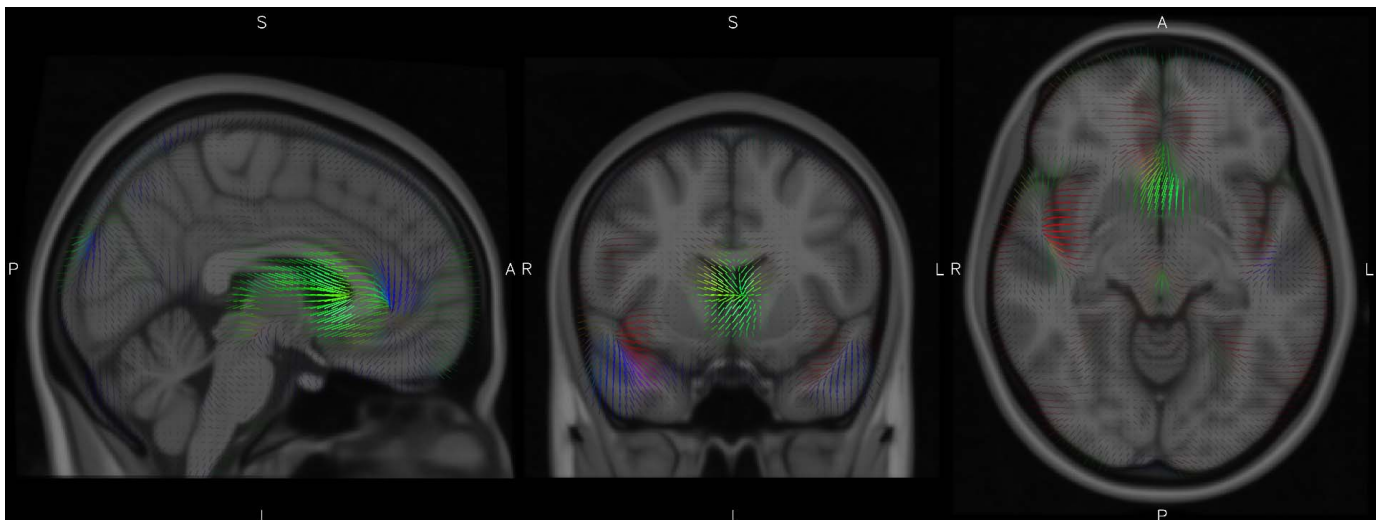


Fig. 7. Long-term average of cardiovascular pulse propagation in human brain across multiple subjects overlaid on MNI standard anatomical images. Stick lengths are proportional to speed, and 3D direction coordinates are represented on RGB color space, as explained in Fig. 6. Intuitively, mixed colors are representing non-orthogonal dominant directions. The intersection of the three planes is at 1-mm MNI coordinate (86, 135, 63), and direction labels L, R, A, P, S, I are standing for left, right, anterior, posterior, superior, inferior, respectively.

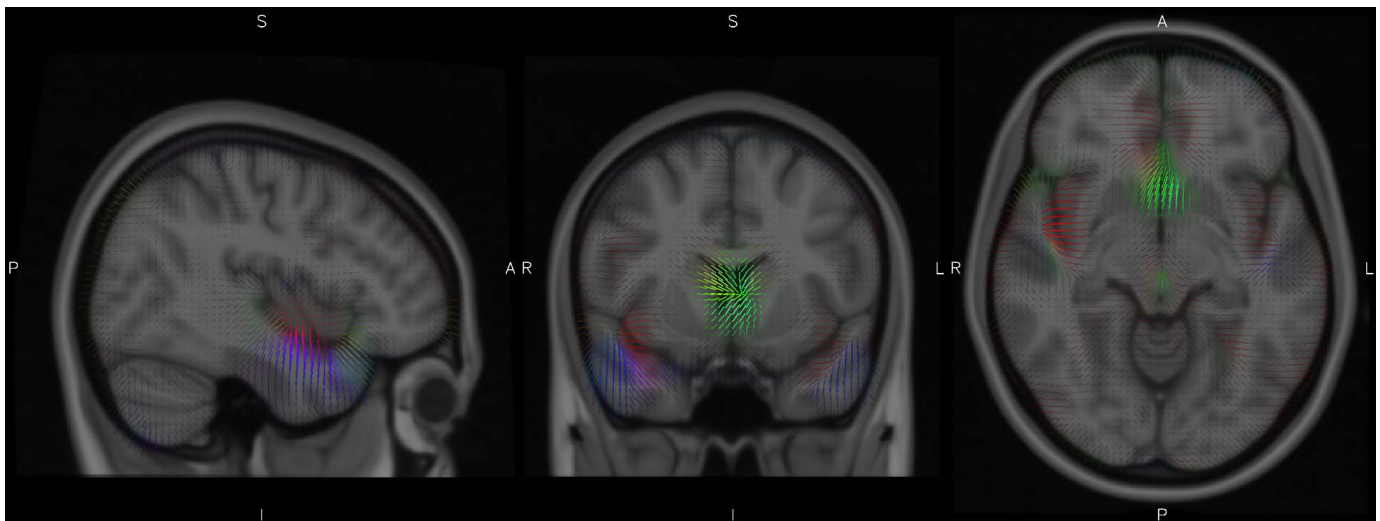


Fig. 8. Long-term average of cardiovascular pulse propagation in human brain across multiple subjects overlaid on MNI standard anatomical images. Stick lengths are proportional to speed, and 3D direction coordinates are represented on RGB color space, as explained in Fig. 6. Intuitively, mixed colors are representing non-orthogonal dominant directions. The intersection of the three planes is at 1-mm MNI coordinate (48, 135, 63), and direction labels L, R, A, P, S, I are standing for left, right, anterior, posterior, superior, inferior, respectively.

CSF spaces conduct the largest proportion of the pulse wave energy, especially the lateral and 3rd CSF ventricles seem to collect a major share of pericallosal arterial impulse back towards the ventricles. CSF cisterns around basilar artery conduit the pulses forward and up from the basal areas. This reflects exactly the pumping mechanism of the central CSF areas.

Interestingly, the pulses entering the ventricles seem to traverse the thalamus and other deep grey matter structures and also sweep the highest areas of the brain stem. The pontine pulses seem to go in AP direction mostly and originate from the 4th ventricle. The pulses in the cerebellum are going to lateral directions from the midline also from the 4th ventricle.

In insula, inter-hemispheric fissure and in Sylvian fissure the pulses seem to dive from the CSF spaces into the brain tissue.

In insula and on both sides of the interhemispheric fissure, the pulses propagate laterally, while in the Sylvian fissure, the pulses seem to surge from the fissure and dive laterally and downwards. Notably in the cortex the pulse vectors follow the anatomy of the sulci very accurately.

After entering the cortex, the pulse propagation speeds shown by the lengths of the vectors dampen quickly as a function of the distance from the CSF space. Within the brain, the sulci seem to conduct the pulses. After reaching the white matter, the pulses seem to vanish suiting the mice results of glymphatic CSF clearance.

There is a corona of cardiovascular pulses all around the edge of the brain extending from the sulcal CSF space outwards. The corona stems from the reflection of the cardiovascular pulse as the pulse bounces from the dural/bone surface

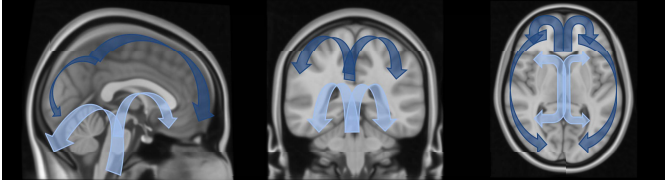


Fig. 9. Schematic figure of coarse cardiovascular pulse propagation paths as described earlier in [6]. Latency of light blue, and dark blue paths from R peak are 500-600 ms, and 700-1000 ms, respectively.

TABLE II

MNI COORDINATES (MM) OF DIAGONAL CUBOID CORNERS

Ventricle area	Right, posterior, inferior corner	Left, anterior, superior corner
Left front plane	(95, 158, 65)	(115, 160, 85)
Left mid plane	(92, 122, 83)	(106, 124, 97)
Right front plane	(65, 158, 65)	(85, 160, 85)
Right mid plane	(74, 122, 83)	(88, 124, 97)

of the cranial vault. This corona is only perturbed by sagittal sinus in the midline where the pulses are drained and twisted toward the sinus. The cerebellum only has such a corona at the dorsal edges but not at the frontal edges against the mastoid bone interface.

B. Pulse Dynamics—Altered in Alzheimer's Disease

We also demonstrate the feasibility of this method to extract information on cardiovascular pulse propagation speed in AD. As presented in the introduction, the cardiovascular pulses are driving the brain clearance, the glymphatic system. Therefore, we expect differences in our measured dynamic properties in AD, since the glymphatic system is not expected to be functioning perfectly. Such a difference in cardiovascular pulse propagation in Alzheimer's disease has not yet been shown in the human brain with MRI.

To keep this example simple, we are focusing on propagation speed with omitting directional information, and we are considering the lateral ventricles of the brain. This is the result of our visual observation, i.e. that the CSF pulsation in ventricles of subjects with AD is altered. This observation is in alignment with cardiovascular pulse propagation results in [6]. The cardiovascular circulation observed in [6] is shown in Fig. 9.

We have constructed a weighted spatial sum signal of the pulse propagation vectors in the full lateral ventricles using the probability maps of the Harvard-Oxford cortical structural atlas [33] as weights, left and right side separately. Furthermore, we used the spatial sum of manually selected planes in front of the left and right ventricles, and in the middle of the left and right ventricles. The MNI coordinates (1 mm) of these cuboids are shown in Table II. Welch's unpaired t-test [34] was used to compare measured properties of control and AD subjects.

With spatial summing, we got time signals representing the different areas, and two properties were calculated for each of these time signals: coefficient of variation ($CV = \frac{std}{mean}$) and sample entropy (SE).

Statistically significant differences between control subjects (con.) and subjects with Alzheimer's disease (pat.) of these properties are shown in Tables III and IV.

TABLE III

COEFFICIENT OF VARIATION DIFFERENCES OF FLOW SPEED IN LATERAL VENTRICLES

Mask	Relation	P-value	95% CI
Left front plane	con.<pat.	4.772e-02	(0.0006553; 0.1099)
Left mid plane	con.<pat.	2.421e-05	(0.05403; 0.1180)
Full left	con.<pat.	1.664e-04	(0.04262; 0.1098)
Right front plane	con.<pat.	2.330e-02	(0.01076; 0.1222)
Full right	con.<pat.	4.169e-02	(0.002094; 0.09771)

TABLE IV

SAMPLE ENTROPY DIFFERENCES OF FLOW SPEED IN LATERAL VENTRICLES

Mask	Relation	P-value	95% CI
Left mid plane	con.>pat.	1.859e-03	(0.08511; 0.2916)
Full left	con.>pat.	8.012e-04	(0.07113; 0.2142)

The same results are also visualized in Fig. 10 as box plots, and even the combinations not yielding statistically significant differences have clear tendencies in lateral ventricles: SE decreases in AD, while CV increases. Thumbnail images of the masks defined in Table II are shown on top of each column.

IV. DISCUSSION

Average directional maps of cardiovascular pulse propagation have been shown for the first time. Details of other anatomical areas (sagittal sections) are provided as a supplementary video. The anatomical accuracy of this method could be useful in generating a directional map for every step of an average cardiac cycle in the future. The images in Fig. 7 and 8 were generated from nearly 30,000 whole brain vector fields. In future work, this data would be interesting to be combined with glymphatic MRI [11], [12], which focuses on longer term effects, and MR brain elastography [35], for analysis of dynamic properties.

Our results show that in the lateral ventricles, SE decreases, and CV increases in Alzheimer's disease. These results match our observation: that cardiovascular pulses are more likely to bounce back and forth in the CSF of lateral ventricles in AD. This phenomenon inherently has more repetition, which explains the smaller entropy measured on the propagation speed in this area. Higher entropy, i.e. a more random propagation might enable the mechanisms of brain clearance in a more evenly distributed way, which is likely to be more efficient on the long term.

Pulse propagation speed for ventricles in AD has higher CV, which means increased variance relative to the mean speed, i.e. relative to the amount of net flow in the area. A straightforward explanation is again the bouncing CSF, which results in a lot of variance (changing propagation direction and high amplitudes), while the overall net flow remains relatively low. The low net flow probably again results in less efficient brain clearance. Both dynamic properties show a reduced compliance of the brain in AD. Further investigation of pulse propagation in AD is necessary to conclude in a more accurate model of the disease. Comparison with other research connecting physiological pulsations and CSF flow, e.g. [3], [13], and [14], is also worthwhile in the future.

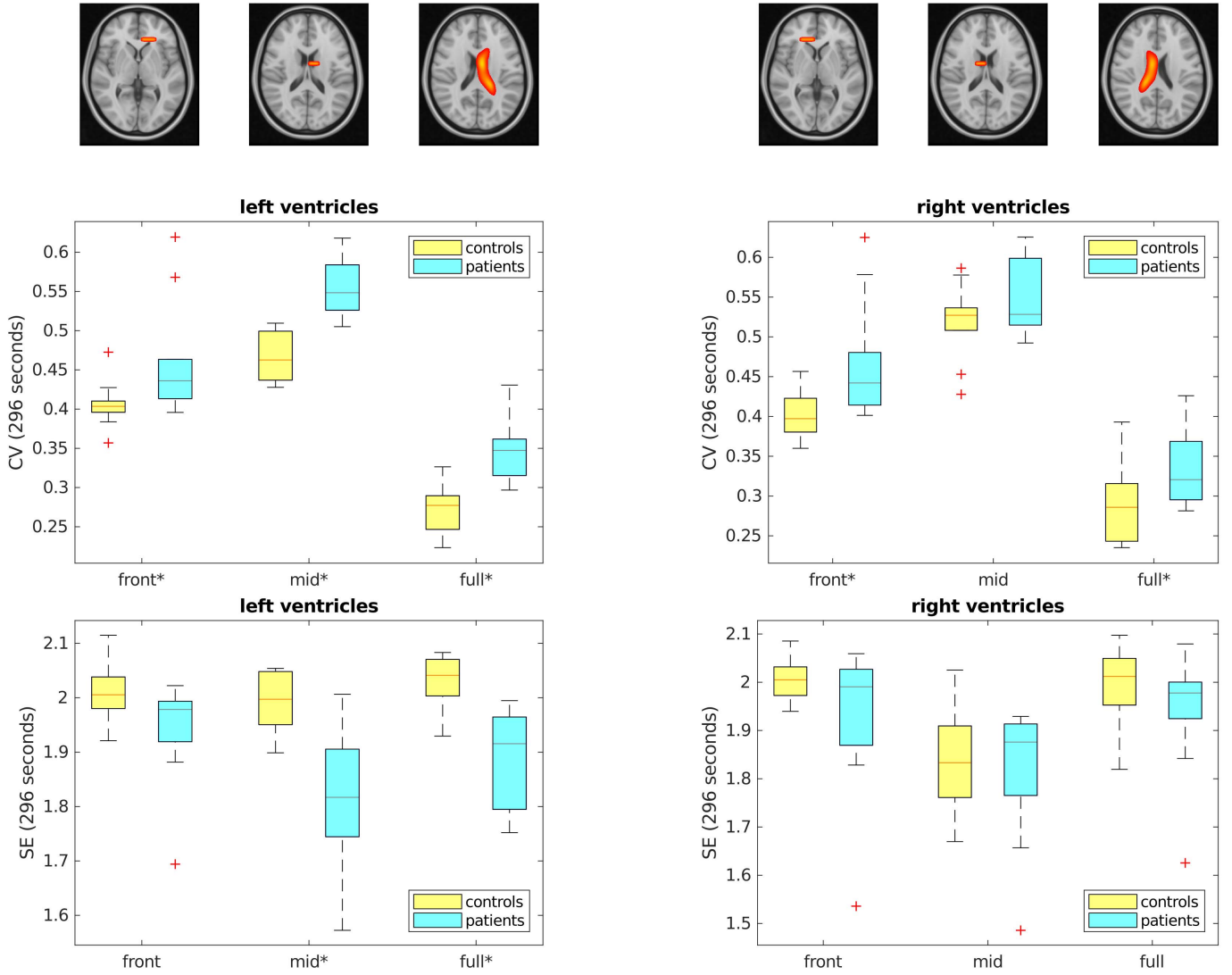


Fig. 10. Coefficient of variation (CV, upper row) and sample entropy (SE, lower row) of cardiovascular pulse speed in lateral ventricles are presented as box plots. Control subjects are shown with yellow, AD subjects with light blue. On top of each column, the focus areas (defined in Table II) are shown on anatomical thumbnails in color. The six columns from left to right are the following: left front plane, left mid plane, full left, right front plane, right mid plane, full right. Where a label is marked with asterisk (*) on horizontal axis, the difference between control and AD subjects is statistically significant ($p < 0.05$).

The accuracy limitations are presented in section II-F: the propagation speed of cardiovascular pulses can be adequately measured with our method at least up to $\frac{17.1 \times 3 \text{ mm}}{0.1 \text{ s}} > 0.5 \frac{\text{m}}{\text{s}}$ flow speed. However, LK method for estimating optical flow (object displacement between consecutive images) is considered simple, and many modern alternatives are available for future improvement. Our choice was made due to the well-known features and limitations, and the fairly short processing time. Calculation speed is an important aspect in processing large MREG data with three native spatial dimensions, and its twenty times faster sampling rate compared to classical FMRI sequences. The focus of this work was to present our novel method, and show a useful example demonstrating its potential. Consequently, robustness of our method was not extensively tested for this specific application, we relied on the fact, that our algorithm consists of solid and time-proven building blocks.

The algorithm presented in this study can estimate the cardiovascular pulse propagation in the human brain, and therefore measure an indicator of brain clearance mechanisms. Measuring such a new dynamic property in the living human brain has great potential. It helps the research community to get closer of solving the still undiscovered mechanisms leading to those neurodegenerative diseases, which are connected to brain clearance impairment.

V. CONCLUSION

We have proposed a novel method to extract cardiovascular wavefront propagation in the brain with a multi-resolution optical flow measurement. By introducing novel dynamic properties of the cardiovascular system in the living human brain, this research has an impact on understanding the development mechanisms of diseases related to brain clearance

impairment. Changes have been shown with our method in Alzheimer's disease. This research opens a window for several neurodegenerative diseases, to discuss their effect on the cardiovascular dynamics in the human brain.

APPENDIX

Extension of Fig. 7 and 8 is provided as a supplementary video. The video provides a walkthrough of sagittal planes on the right side of the brain. The planes are provided between 1 mm MNI coordinates (30, 135, 63) and (90, 135, 63).

REFERENCES

- [1] M. Nedergaard, "Garbage truck of the brain," *Science*, vol. 340, no. 6140, pp. 1529–1530, Jun. 2018. doi: [10.1126/science.1240514](https://doi.org/10.1126/science.1240514).
- [2] J. J. Iliff *et al.*, "A paravascular pathway facilitates CSF flow through the brain parenchyma and the clearance of interstitial solutes, including amyloid β ," *Sci. Transl. Med.*, vol. 4, no. 147, Aug. 2012, Art. no. 111. doi: [10.1126/scitranslmed.3003748](https://doi.org/10.1126/scitranslmed.3003748).
- [3] H. Mestre *et al.*, "Flow of cerebrospinal fluid is driven by arterial pulsations and is reduced in hypertension," *Nature Commun.*, vol. 9, no. 1, Nov. 2018, Art. no. 4878. doi: [10.1038/s41467-018-07318-3](https://doi.org/10.1038/s41467-018-07318-3).
- [4] J. J. Iliff *et al.*, "Cerebral arterial pulsation drives paravascular CSF–interstitial fluid exchange in the murine brain," *J. Neurosci.*, vol. 33, no. 46, pp. 18190–18199, Nov. 2013. doi: [10.1523/JNEUROSCI.1592-13.2013](https://doi.org/10.1523/JNEUROSCI.1592-13.2013).
- [5] N. A. Jessen, A. S. F. Munk, I. Lundgaard, and M. Nedergaard, "The glymphatic system: A beginner's guide," *Neurochem. Res.*, vol. 40, no. 12, pp. 2583–2599, Dec. 2015. doi: [10.1007/s11064-015-1581-6](https://doi.org/10.1007/s11064-015-1581-6).
- [6] V. Kiviniemi *et al.*, "Ultra-fast magnetic resonance encephalography of physiological brain activity—Glymphatic pulsation mechanisms?" *J. Cerebral Blood Flow Metabolism*, vol. 36, no. 6, pp. 1033–1045, Jun. 2016. doi: [10.1177/0271678X15622047](https://doi.org/10.1177/0271678X15622047).
- [7] A. Burgess *et al.*, "Alzheimer disease in a mouse model: MR imaging-guided focused ultrasound targeted to the hippocampus opens the blood-brain barrier and improves pathologic abnormalities and behavior," *Radiology*, vol. 273, no. 3, pp. 736–745, Sep. 2014. doi: [10.1148/radiol.14140245](https://doi.org/10.1148/radiol.14140245).
- [8] G. Leinenga and J. Götz, "Scanning ultrasound removes amyloid- β and restores memory in an Alzheimer's disease mouse model," *Sci. Transl. Med.*, vol. 7, no. 278, Mar. 2015, Art. no. 33. doi: [10.1126/scitranslmed.aaa2512](https://doi.org/10.1126/scitranslmed.aaa2512).
- [9] N. J. Albargothy *et al.*, "Convective influx/glymphatic system: Tracers injected into the CSF enter and leave the brain along separate periaxonal basement membrane pathways," *Acta Neuropathol.*, vol. 136, no. 1, pp. 139–152, Jul. 2018. doi: [10.1007/s00401-018-1862-7](https://doi.org/10.1007/s00401-018-1862-7).
- [10] I. F. Harrison *et al.*, "Non-invasive imaging of CSF-mediated brain clearance pathways via assessment of perivascular fluid movement with diffusion tensor MRI," *eLife*, vol. 7, Jul. 2018, Art. no. e34028. doi: [10.7554/eLife.34028](https://doi.org/10.7554/eLife.34028).
- [11] G. Ringstad, S. A. S. Vatnehol, and P. K. Eide, "Glymphatic MRI in idiopathic normal pressure hydrocephalus," *Brain*, vol. 140, no. 10, pp. 2691–2705, Oct. 2017. doi: [10.1093/brain/awx191](https://doi.org/10.1093/brain/awx191).
- [12] G. Ringstad *et al.*, "Brain-wide glymphatic enhancement and clearance in humans assessed with MRI," *JCI Insight*, vol. 3, no. 13, Jul. 2018, Art. no. e121537. doi: [10.1172/jci.insight.121537](https://doi.org/10.1172/jci.insight.121537).
- [13] S. Dreha-Kulaczewski, A. A. Joseph, K.-D. Merboldt, H. C. Ludwig, J. Gärtner, and J. Frahm, "Inspiration is the major regulator of human CSF flow," *J. Neurosci.*, vol. 35, no. 6, pp. 2485–2491, Feb. 2015. doi: [10.1523/JNEUROSCI.3246-14.2015](https://doi.org/10.1523/JNEUROSCI.3246-14.2015).
- [14] S. Dreha-Kulaczewski, A. A. Joseph, K.-D. Merboldt, H. C. Ludwig, J. Gärtner, and J. Frahm, "Identification of the upward movement of human CSF *in vivo* and its relation to the brain venous system," *J. Neurosci.*, vol. 37, no. 9, pp. 2395–2402, Mar. 2017. doi: [10.1523/JNEUROSCI.2754-16.2017](https://doi.org/10.1523/JNEUROSCI.2754-16.2017).
- [15] I. Makedonov, J. J. Chen, M. Masellis, B. J. MacIntosh, and Alzheimer's Disease Neuroimaging Initiative, "Physiological fluctuations in white matter are increased in Alzheimer's disease and correlate with neuroimaging and cognitive biomarkers," *Neurobiol. Aging*, vol. 37, pp. 12–18, Jan. 2016. doi: [10.1016/j.neurobiolaging.2015.09.010](https://doi.org/10.1016/j.neurobiolaging.2015.09.010).
- [16] T. Tuovinen *et al.*, "Altered BOLD signal variation in Alzheimer's disease and frontotemporal dementia," *BioRxiv*, Oct. 2018, Art. no. 455683. doi: [10.1101/455683](https://doi.org/10.1101/455683).
- [17] J. Kananen *et al.*, "Altered physiological brain variation in drug-resistant epilepsy," *Brain Behav.*, vol. 8, no. 9, Sep. 2018, Art. no. e01090. doi: [10.1002/brb3.1090](https://doi.org/10.1002/brb3.1090).
- [18] B. D. Lucas and T. Kanade, "An iterative image registration technique with an application to stereo vision," in *Proc. 7th Int. J. Conf. Artif. Intell.*, Vancouver, BC, Canada, vol. 2, Aug. 1981, pp. 674–679.
- [19] B. Zahneisen *et al.*, "Single shot concentric shells trajectories for ultra fast fMRI," *Magn. Reson. Med.*, vol. 68, no. 2, pp. 484–494, Aug. 2012. doi: [10.1002/mrm.23256](https://doi.org/10.1002/mrm.23256).
- [20] H.-L. Lee, B. Zahneisen, T. Hugger, P. LeVan, and J. Hennig, "Tracking dynamic resting-state networks at higher frequencies using MR-encephalography," *NeuroImage*, vol. 65, pp. 216–222, Jan. 2013. doi: [10.1016/j.neuroimage.2012.10.015](https://doi.org/10.1016/j.neuroimage.2012.10.015).
- [21] J. Assländer *et al.*, "Single shot whole brain imaging using spherical stack of spirals trajectories," *NeuroImage*, vol. 73, pp. 59–70, Jun. 2013. doi: [10.1016/j.neuroimage.2013.01.065](https://doi.org/10.1016/j.neuroimage.2013.01.065).
- [22] F.-H. Lin, L. L. Wald, S. P. Ahlfors, M. S. Hämäläinen, K. K. Kwong, and J. W. Belliveau, "Dynamic magnetic resonance inverse imaging of human brain function," *Magn. Reson. Med.*, vol. 56, no. 4, pp. 787–802, Oct. 2006. doi: [10.1002/mrm.20997](https://doi.org/10.1002/mrm.20997).
- [23] F.-H. Lin *et al.*, "K-space reconstruction of magnetic resonance inverse imaging (K-InI) of human visuomotor systems," *NeuroImage*, vol. 7, no. 4, Aug. 2013, Art. no. 479. doi: [10.1016/j.neuroimage.2009.11.016](https://doi.org/10.1016/j.neuroimage.2009.11.016).
- [24] S. Posse *et al.*, "High-speed real-time resting-state FMRI using multi-slab echo-volumar imaging," *Front. Hum. Neurosci.*, vol. 7, Aug. 2013, Art. no. 479. doi: [10.3389/fnhum.2013.00479](https://doi.org/10.3389/fnhum.2013.00479).
- [25] M. F. Folstein, S. E. Folstein, and P. R. McHugh, "Mini-mental state: A practical method for grading the cognitive state of patients for the clinician," *J. Psychiatric Res.*, vol. 12, no. 3, pp. 189–198, Nov. 1975. doi: [10.1016/0022-3956\(75\)90026-6](https://doi.org/10.1016/0022-3956(75)90026-6).
- [26] V. Korhonen *et al.*, "Synchronous multiscale neuroimaging environment for critically sampled physiological analysis of brain function: heptascan concept," *Brain Connect.*, vol. 4, no. 9, pp. 677–689, Nov. 2014. doi: [10.1089/brain.2014.0258](https://doi.org/10.1089/brain.2014.0258).
- [27] M. Jenkinson, P. Bannister, M. Brady, and S. Smith, "Improved optimization for the robust and accurate linear registration and motion correction of brain images," *NeuroImage*, vol. 17, no. 2, pp. 825–841, Oct. 2002. doi: [10.1006/nimg.2002.1132](https://doi.org/10.1006/nimg.2002.1132).
- [28] S. M. Smith, "Fast robust automated brain extraction," *Human Brain Mapping*, vol. 17, no. 3, pp. 143–155, 2002. doi: [10.1002/hbm.10062](https://doi.org/10.1002/hbm.10062).
- [29] C. F. Beckmann and S. M. Smith, "Probabilistic independent component analysis for functional magnetic resonance imaging," *IEEE Trans. Med. Imag.*, vol. 23, no. 2, pp. 137–152, Feb. 2004. doi: [10.1109/TMI.2003.822821](https://doi.org/10.1109/TMI.2003.822821).
- [30] R. W. Cox, "AFNI: Software for analysis and visualization of functional magnetic resonance neuroimages," *Comput. Biomed. Res.*, vol. 29, no. 3, pp. 162–173, 1996.
- [31] P. E. Danielsson, and O. Seger, "Generalized and separable Sobel operators," in *Machine Vision for Three-Dimensional Scenes*, H. Freeman, Ed. New York, NY, USA: Academic, 1990, pp. 347–379. doi: [10.1016/B978-0-12-266722-0.50016-6](https://doi.org/10.1016/B978-0-12-266722-0.50016-6).
- [32] J. R. Bergen, P. Anandan, K. J. Hanna, and R. Hingorani, "Hierarchical model-based motion estimation," in *Proc. 2nd Eur. Conf. Comput. Vis.*, Santa Margherita Ligure, Italy, May 1992, pp. 237–252.
- [33] R. S. Desikan *et al.*, "An automated labeling system for subdividing the human cerebral cortex on MRI scans into gyral based regions of interest," *NeuroImage*, vol. 31, no. 3, pp. 968–980, Jul. 2006. doi: [10.1016/j.neuroimage.2006.01.021](https://doi.org/10.1016/j.neuroimage.2006.01.021).
- [34] B. L. Welch, "The generalization of 'student's' problem when several different population variances are involved," *Biometrika*, vol. 34, nos. 1–2, pp. 28–35, 1947. doi: [10.1093/biomet/34.1-2.28](https://doi.org/10.1093/biomet/34.1-2.28).
- [35] M. C. Murphy, J. Huston, III, and R. L. Ehman, "MR elastography of the brain and its application in neurological diseases," *NeuroImage*, vol. 187, pp. 176–183, Oct. 2017. doi: [10.1016/j.neuroimage.2017.10.008](https://doi.org/10.1016/j.neuroimage.2017.10.008).